BAMS Article

Diverse MJO Genesis and Predictability

Yuntao Wei, Hong-Li Ren, Baoqiang Xiang, Yan Wang, Jie Wu, and Shuguang Wang

ABSTRACT: The Madden–Julian oscillation (MJO) is the dominant intraseasonal wave phenomenon influencing extreme weather and climate worldwide. Realistic simulations and accurate predictions of MJO genesis are the cornerstones for successfully monitoring, forecasting, and managing meteorological disasters 3–4 weeks in advance. Nevertheless, the genesis processes and emerging precursor signals of an eastward-propagating MJO event remain largely uncertain. Here, we find that the MJO genesis processes observed in the past four decades exhibit remarkable diversity with different seasonality and can be classified objectively into four types, namely, a novel downstream origin from the westward-propagating intraseasonal oscillation (WPISO; 20.4%), localized breeding from the Indian Ocean suppressed convection (IOSC; 15.4%), an upstream succession of the preceding weakly dispersive (WD; 25.9%), and strongly dispersive (SD; 38.3%) MJO. These four types are associated with different oceanic background states, characterized by central Pacific cooling, southern Maritime Continent warming, eastern Pacific cooling, and central Pacific warming for the WPISO, IOSC, WD, and SD types, respectively. The SD type is also favored during the easterly phase of the stratospheric quasi-biennial oscillation. Diverse convective initiations possibly imply various kinds of propagations of MJO. The subseasonal reforecasts indicate robustly distinct prediction skills for the diverse MJO genesis. A window of opportunity for skillful week 3–4 prediction probably opens with the aid of the WPISO-type MJO precursor, which has increased the predictability of primary MJO onset by 1 week. These findings suggest that the diversified MJO genesis can be skillfully foreseen by monitoring unique precursor signals and can also serve as benchmarks for evaluating contemporary models' modeling and predicting capabilities.

KEYWORDS: Madden-Julian oscillation; Sea surface temperature; Forecast verification/skill; Quasibiennial oscillation; Communications/decision making; Clustering

https://doi.org/10.1175/BAMS-D-22-0101.1
Corresponding author: Hong-Li Ren, renhl@cma.gov.cn
Supplemental material: https://doi.org/10.1175/BAMS-D-22-0101.2

In final form 19 February 2023

AFFILIATIONS: Wei—State Key Laboratory of Severe Weather, and Institute of Tibetan Plateau Meteorology, Chinese Academy of Meteorological Sciences, Beijing, and Collaborative Innovation Center on Forecast and Evaluation of Meteorological Disasters, Nanjing University of Information Science and Technology, Nanjing, and Department of Atmospheric and Oceanic Sciences and Institute of Atmospheric Sciences, CMA-FDU Joint Laboratory of Marine Meteorology, Fudan University, Shanghai, and LASG, Institute of Atmospheric Physics, Chinese Academy of Sciences, Beijing, China; **Ren**—State Key Laboratory of Severe Weather, and Institute of Tibetan Plateau Meteorology, Chinese Academy of Meteorological Sciences, Beijing, and Collaborative Innovation Center on Forecast and Evaluation of Meteorological Disasters, Nanjing University of Information Science and Technology, Nanjing, China; **Xiang**—NOAA/Geophysical Fluid Dynamics Laboratory, Princeton, New Jersey, and University Corporation for Atmospheric Research, Boulder, Colorado; **Wang**—Shanxi Climate Center, Xi'an, Shanxi, China; **Wu**—CMA Climate Studies Key Laboratory and CMA-NJU Joint Laboratory for Climate Prediction Studies, National Climate Center, China Meteorological Administration, Beijing, China; **Wang**—School of Atmospheric Sciences, and Key Laboratory of Mesoscale Severe Weather/Ministry of Education, Nanjing University, Nanjing, China

In the tropics, the organization and propagation of convective clouds occur at various spatiotemporal scales (Waliser et al. 2012). In favorable environments, for example, the mesoscale cloud systems, which usually arise from the upscale growth of cumulus clouds over the ocean or land/coastal regions (Yang and Slingo 2001), can organize into synoptic-scale super cloud clusters (SCCs; Nakazawa 1988). With an average recurrence period of 30–60 days, these SCCs may grow further and build a planetary-scale envelope propagating slowly eastward (~5 m s^{-1}) over warm oceans (Zhang 2005). Nowadays, we know this phenomenon as the tropical intraseasonal oscillation, first mentioned by Xie et al. (1963) and named the Madden–Julian oscillation (MJO) after the pioneering works by Madden and Julian (1971, 1972).

Since its discovery, the MJO remains a frontier research topic as it profoundly affects extreme weather and climate phenomena worldwide (Zhang 2013), such as onsets and breaks of the Asian–Australian monsoon (Yasunari 1980; Lau and Chan 1986; Hendon and Liebmann 1990), the genesis of typhoons and hurricanes (Liebmann et al. 1994; Maloney and Hartmann 2000), rainfall extremes and droughts (Ren and Ren 2017; Wang et al. 2022), heat and cold waves (Matsueda and Takaya 2015), the teleconnections of the Pacific–North American pattern (Zhou et al. 2020; Wei and Ren 2022) and North Atlantic Oscillation (Cassou 2008), sudden stratospheric warming (Garfinkel et al. 2012), East Antarctic cooling (Hsu et al. 2021), and atmospheric rivers (Mundhenk et al. 2018). The MJO can also influence the underlying ocean by altering sea surface momentum, heat, and freshwater fluxes (Moum et al. 2016). In particular, the MJO can even trigger or terminate El Niño–Southern Oscillation (McPhaden 1999; Takayabu et al. 1999) and Indian Ocean dipole (Rao and Yamagata 2004). Moreover, MJO largely sources the subseasonal-to-seasonal predictability (Waliser et al. 2003) and is pivotal for the implementation of seamless prediction by bridging medium-range weather forecasting and short-term seasonal climate prediction (Zhang 2013).

Despite the tremendous economic and societal importance of the MJO, our understanding of its fundamentals is still subject to debate. The conceptual picture of the MJO contains the so-called "skeleton" that mimics the most salient features of the canonical MJO, including intraseasonal and planetary scales and slow eastward propagation (Zhang et al. 2020; Jiang et al. 2020). However, the observed MJOs are diverse, with large event-to-event differences

(Bellenger and Duvel 2012; Pohl and Camberlin 2014). Previous studies mainly investigated the diversity of MJO propagation (e.g., Wei and Ren 2019; Wang et al. 2019; Xiang et al. 2022), while less attention has been paid to the preconditioning stage of an MJO (Matthews 2008). A better understanding of the various genesis processes of the MJO is so vital that we might identify precursor signals days in advance and use them to monitor and predict the onset type of the coming new MJO. Moreover, the prediction accuracy for the leading time of 3–4 weeks not only depends on the good prediction of MJO propagation but also benefits from the reliable MJO genesis forecast. None of the popular MJO theories can faithfully reproduce the episodic genesis nature of the observed MJO (Zhang 2005; Zhang and Yoneyama 2017), implying that our current understanding of the MJO genesis/onset (see sidebar for its definition) remains limited (Zhang et al. 2020).

Many efforts have been made to explore MJO initiation, such as the international and unprecedented Dynamics of the MJO field campaign over the Indian Ocean (IO) during the boreal winter of 2011/12 (Yoneyama et al. 2013). Owing to the prevalence of the descending branch of Walker cell over the western IO, the lower troposphere must be sufficiently moistened to prompt the initiation of deep convection that eventually develops into an MJO envelope (Zhang and Yoneyama 2017). Regarding the sources of lower-tropospheric moistening and equivalent destabilization, there are currently two main groups of views, i.e., the MJO genesis is in the tropics through the localized moist energy recharge (Kemball-Cook and Weare 2001; Takasuka et al. 2018; Wei et al. 2019, 2020) or by the succession of the preceding MJO (Matthews 2000, 2008), while in the second group, the role of extratropical disturbances is highlighted (Matthews and Kiladis 1999; Zhao et al. 2013).

These previous works have alluded to the possible initiation mechanisms of the MJO. In this study, we examine the MJO events originating over the IO, where more than 70% of the observed MJO events when identified using precipitation were generated (Zhang and Ling 2017). Note that this percentage may differ from that using other variables, such as outgoing longwave radiation (e.g., Kiladis et al. 2014; Stachnik and Chrisler 2020). Due to modulation of the interannual sea surface temperature (SST) variability, the MJO deep convection might be triggered over the Maritime Continent and the western Pacific. However, these cases were excessively few (Takasuka and Satoh 2021), and thus they are not considered in this research. We aim to classify the disordered intraseasonal convective anomalies in the deep tropics preceding the onset of eastward-propagating MJO events. This is in line with the preference of meteorologists who usually monitor or forecast the MJOs based on the Hovmöller diagrams of equatorially averaged (15°S–15°N) convection signals and the classical MJO indices (Wheeler and Hendon 2004). In this study, we would like to propose several key precursor signals of diverse MJO genesis modulated by different oceanic and stratospheric background states.

Definition of MJO onset

Accurately defining MJO onset or genesis is not easy since the definition of the MJO itself is even controversial (Straub 2013). Many indices have been previously proposed to characterize the MJOs, including those based on cloudiness (Matthews 2008; Kiladis et al. 2014), circulations (Adames and Kim 2016), and combined cloudiness and circulations (Wheeler and Hendon 2004). The most typical feature of the MJOs may be the slow eastward propagation of large-scale wave envelopes of organized cloud clusters in the tropics (Jiang et al. 2020; Zhang et al. 2020). The appearance of this phenomenon in the IO is usually regarded as the MJO onset or genesis (Zhang and Yoneyama 2017). For instance, as presented in Fig. 1, the composites of the 20–100-day filtered OLR (a proxy for the cloudiness) in the four clusters show a large-scale eastward-propagating wave after day 0, which indicates the MJO onset. MJO onset is usually accompanied by moisture accumulation from the bottom to the tropopause (Wei and Pu 2021). Therefore, moisture accumulation processes are crucial for investigating the mechanisms of MJO onset in the IO (Yoneyama et al. 2013).

More importantly, we expect to detect a time window with a high probability to achieve a better week 3–4 prediction of the MJO (Mariotti et al. 2020) based on the unique precursor signals of MJO genesis.

Diversity of MJO genesis

An objective mode-based identification method, namely, *k*-means cluster analysis from big data ensembles (Hartigan and Wong 1979), has been recently used to examine the variation of MJO propagation during boreal winter (Wang et al. 2019; Xiang et al. 2022). However, a full MJO life cycle also includes the preconditioning stage, and the subseasonal prediction may be improved by detecting diverse MJO genesis and its precursor signals. Thus, the *k*-means cluster analysis is applied to classify the generation processes of 201 observed MJO events originating from the IO during 1980–2020 (introduced in appendix A). Different from Wang et al. (2019), we perform the clustering analysis focusing on the convection anomalies preceding the MJO onset (i.e., day −30 to day 0, where day 0 indicates the time when the MJO convection reaches the peak in the IO). The MJO genesis is divided into four clusters (see appendix B for method details). This classification is an extension of Matthews (2008) and is intrinsically different from that of the MJO with diverse initiation regions (Takasuka and Satoh 2021). Also, the classification differs from that of considering only successive[1] MJO events with distinct tropical and extratropical triggers (Zhao et al. 2013).

[1] The terminology "successive MJO" denotes a kind of MJO episode with an immediately preceding MJO. The remaining episodes are the "primary MJO," which occurs without an immediately preceding MJO (Matthews 2008).

The first cluster, accounting for 20.4% of all MJO events, is categorized as the westward-propagating intraseasonal oscillation (WPISO) since there exists significant westward-propagating deep convection preceding the MJO onset over the IO (Fig. 1a). The WPISO signals might source from equatorial Rossby waves (Fig. ES1 in the online supplemental material) and can be observed more clearly from the column-integrated water vapor (CWV) anomalies, which show spatiotemporal variations consistent with the outgoing longwave radiation (OLR). The moist WPISO is trailed by an apparent dry convection anomaly in the western Pacific that occurs about 15 days before the MJO onset and propagates westward to the western Maritime Continent (~120°E). Moreover, note that localized convection suppression appears on the twentieth day before the MJO (denoted as day −20, same as below) in the central-eastern IO. The phase diagrams of the real-time multivariate MJO (RMM; Wheeler and Hendon 2004) index and OLR-based MJO index (OMI; Kiladis et al. 2014) indicate that the MJO initiation in the WPISO cluster is primary, i.e., the indexes evolve outward from inside the unit circle (Fig. ES2a). The WPISO type resembles the "initial westward" Madden–Julian (MJ) events in Matthews (2008). However, for the initial westward MJ events, the preceding westward-propagating signals occur over Indonesia rather than the central Pacific for the WPISO type.

The second cluster covers 15.4% of all MJO events. The composite OLR and CWV anomalies manifest a robust eastward propagation from the IO to the western Pacific, with a faster speed than the WPISO-triggered MJO (Fig. 1b). Before the onset of the MJO deep convection, there is little obvious signal except for a localized convection suppression over the IO on around day −15, which is reminiscent of the canonical primary MJO event investigated first by Matthews (2008). Likewise, the primality shown in the RMM and OMI phase diagrams suggests a clear MJO evolution from weak to strong (Fig. ES2b). According to the unique characteristics of the processes of MJO genesis, this cluster is classified as the IO suppressed convection (IOSC). The WPISO and IOSC members together constitute all the primary MJOs originating from the IO during the past four decades, accounting for about 35% of the total, which is consistent with the findings of Snide et al. (2021).

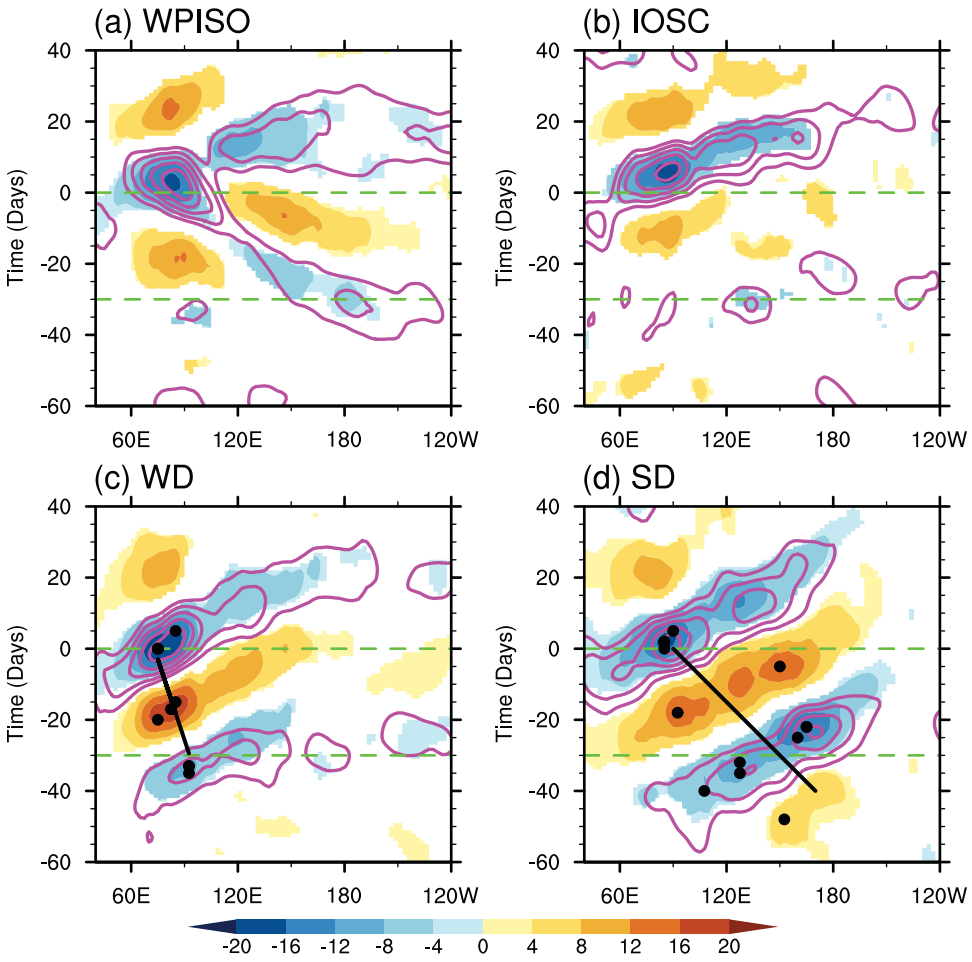

Fig. 1. MJO genesis diversity over the IO. Composite 20–100-day filtered, equatorially averaged (15°S–15°N) anomalies of outgoing longwave radiation (OLR) (W m^{-2}; shading) and column-integrated water vapor (CWV) (contours; g kg^{-1}) in the (a) westward-propagating intraseasonal oscillation (WPISO), (b) IO suppressed convection (IOSC), (c) weakly dispersive (WD), and (d) strongly dispersive (SD). CWV is only shown for positive anomalies larger than 0.05 g kg^{-1} with an interval of 0.05 g kg^{-1}. Shaded areas present the OLR passing the significance Student's *t* test at the 95% confidence level. The *k*-means clustering analysis focuses on the time interval of day –30 to day 0, which is represented by the two dashed green lines. The black lines in (c) and (d) show the energy dispersion of wave envelopes before MJO genesis, derived from the linear least squares fitting of black circles that represent local extrema at 10-day intervals with 5-day overlap (see Text ES2 in the online supplemental material).

The remaining ~65% belong to successive MJO events, which can be further divided into two clusters based on the distinct processes of convection genesis, namely, upstream succession from weak dispersive (WD; Fig. 1c) and strong dispersive (SD; Fig. 1d) preceding MJO. For example, the wave envelopes for the SD cluster before MJO onset feature a strong westward energy dispersion, with a group velocity of about –2.5 m s^{-1} (evaluated based on the methods of Adames and Kim 2016). In the WD cluster, the energy dispersion is weak, and the group velocity is only –0.7 m s^{-1}. Detailed explanations of the wave dispersion and group velocity as well as the possible physical mechanisms in the WD versus SD types are given in the supplemental Text ES2. Compared with the WD cluster, the SD cluster has a faster propagation from the IO to the Maritime Continent, with a stronger convection intensity over the western Pacific. Additionally, the composite RMM and OMI indexes of the SD cluster (Fig. ES2d) are slightly stronger than those of the WD cluster (Fig. ES2c). Several MJO theories predicted an analog of the WD cluster (Majda and Stechmann 2009; Yang and Ingersoll 2013; Wang et al. 2016), while the "moisture-mode" theory predicted a dispersive MJO similar to the SD type (Sobel and Maloney 2013; Adames and Kim 2016).

The observational coexistence of these two clusters, with the WD and SD members accounting for about 25.9% and 38.3% of the total MJOs, strongly demonstrates the joint role of the two theories in explaining a portion of the MJO events. This also reminds us that, besides the WD-type MJO genesis, new theoretical models of the MJO should also be able to reproduce the SD-type MJO.

The diverse MJO genesis may also feature different seasonality. To address this issue, we count the number of the occurrence month of day 0 in each MJO genesis type. Seen from the radar chart shown in Fig. 2, diverse seasonal distributions of MJO genesis are evident. For example, WPISO and IOSC types mostly occur during the boreal summer, with the peak occurrence month in July and June, respectively. In contrast, the occurrence month of successive MJO genesis prefers the boreal winter, peaking in November and February for the WD and SD types, respectively. Different from Matthews (2008), the boreal summer is revealed here as the preferred season of primary MJO initiation. This discrepancy is likely expected since we have examined the data record during 1979–2020, while Matthews (2008) analyzed that

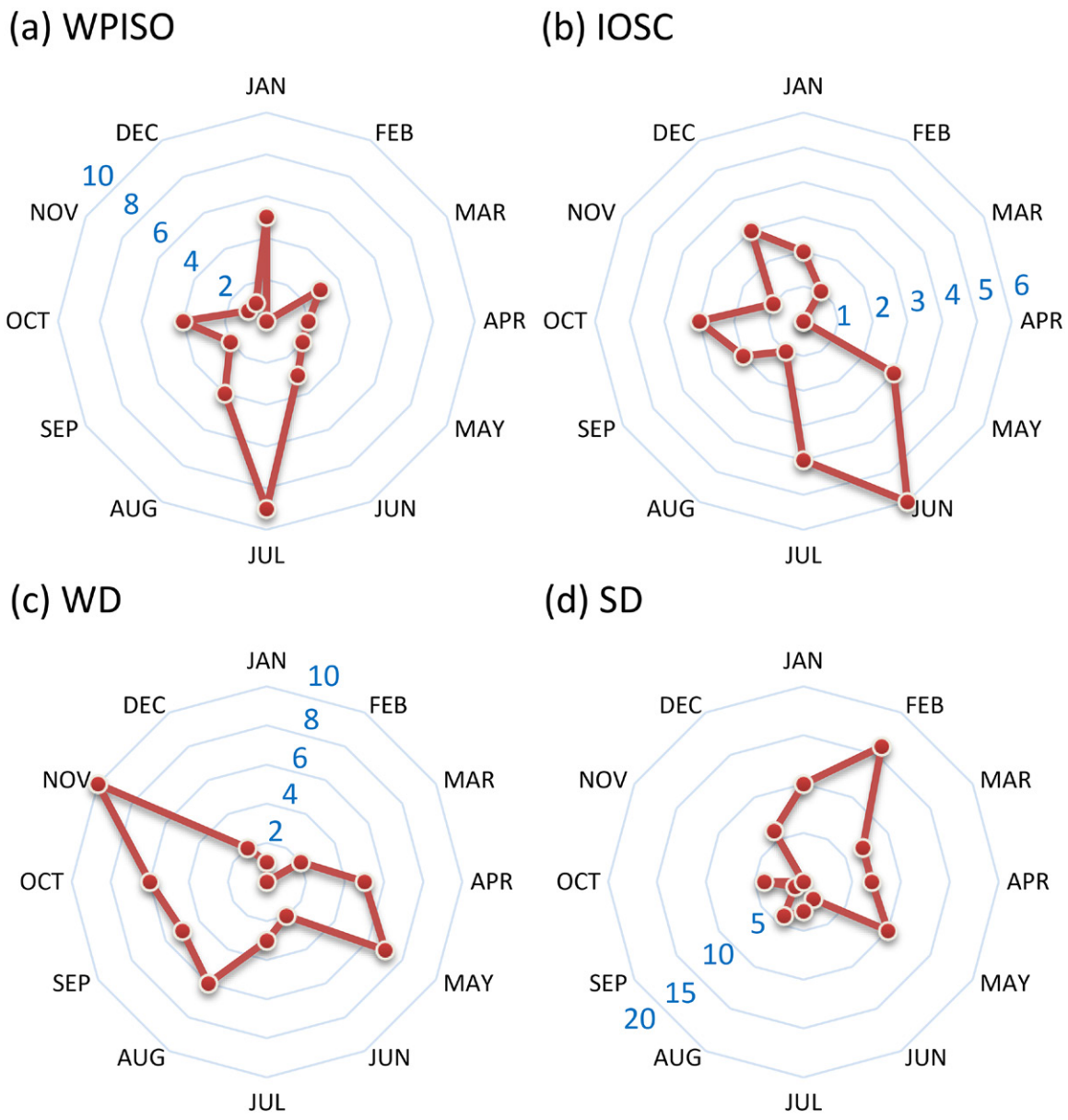

Fig. 2. Seasonality of MJO genesis diversity. Shown are the radar charts of the seasonal distribution of (a) WPISO, (b) IOSC, (c) WD, and (d) SD types of MJO genesis. The red marked line represents the number of the calendar month (January–December) of MJO convective onset on day 0. The reference number of the occurrence month of day 0 in each axis is shown in blue color.

during 1974–2005. However, our results are similar to Yong and Mao (2016), who also used the data record after 1979 to investigate the primary events.

Diverse triggering processes of the MJO

What triggers the MJO onset and what is the fundamental physics behind it? There is extensive literature on the processes of the MJO genesis for the IOSC, WD, and SD types. For example, in terms of the primary events (IOSC type), the triggering factors of the MJOs include cold midtropospheric temperature (Matthews 2008), oceanic Rossby waves (Webber et al. 2010), nonlinear horizontal moisture advection (Wei et al. 2019, 2020), and mixed Rossby–gravity waves (Takasuka et al. 2019, 2021). For the successive events (WD and SD types), the new MJO convection is reinitiated over the IO by the circumnavigation of the preceding MJO, dry Kelvin waves emanating from the preceding MJO (Matthews 2000; Straub et al. 2006), air–sea interaction (Li et al. 2008), and large-scale moisture advection (Zhao et al. 2013). However, a systematic and quantitative classification of the IOSC-, WD-, and SD-type MJO genesis has not yet been investigated. Moreover, there are few studies on the different MJO triggers caused by the preceding MJO with different dispersion, which is practically useful and necessary due to the distinct predictability of the MJO onset for the WD and SD clusters.

For the newly identified WPISO cluster, we attempt to understand the process of MJO genesis from the perspective of circulation-convection coupling, focusing on moisture accumulation (Zhang and Yoneyama 2017). On day −32, the WPISO signal sticks out a moist tongue toward New Guinea (Fig. 3). When encountering the "damping effect" of the Maritime Continent, the moist tongue splits into two parts straddling the equator. The northern part gradually evolves into a cyclonic circulation coupled with moist convection and moves northwestward slowly. The southern part, although slightly weakened in the Maritime Continent but still clearly visible, migrates westward slowly along ~15°S. More interestingly, the northern and southern branches redevelop and merge over the eastern edge of the IO from days −11 to −8 (Fig. ES3), thus contributing to the marked local moisture accumulation, namely, positive CWV tendency. A space–time filtering decomposition (Wheeler and Kiladis 1999) suggested that the moisture signals associated with the equatorial Rossby wave (Fig. ES1) could explain ~60% of the total moisture anomalies over 15°S–10°N, 80°–110°E from days −8 to −5. Feng and Li (2016) also noted that the merged moisture accumulation was partially from the equatorial Rossby wave before a primary MJO event during the boreal winter of 2000/01.

The easterly wind anomalies coupled with suppressed convection in the central IO also partially contribute to the growth of MJO moisture over 15°S–10°N, 70°–100°E (Text ES1). The dry phase of WPISO strengthens the equatorial easterly and poleward wind anomalies through exciting Rossby wave responses over the Maritime Continent. These wind anomalies then activate the eastward propagation of moist convection by moistening the region from the Maritime Continent to the western Pacific due to the poleward moisture advection (Kim et al. 2014; Wei and Ren 2019) and frictional moisture convergence caused by easterly wind anomalies (Wang et al. 2019).

Possible background state controls on MJO genesis diversity

In this section, to reveal the possible controlling effects of background states on the diversity of MJO genesis, we diagnose the monthly anomalies of the SST (SSTA), 850-hPa zonal wind (U850A), and moist static energy (MSEA). The 3-month average SSTA, U850A, and MSEA with lags ranging from −2 to 0 months are calculated as the background state for each MJO genesis, which is different from the average with lags ranging from −1 to +1 month in previous studies that emphasized the diversity of MJO propagation (Wang et al. 2019; Xiang et al. 2022; Wei et al. 2022). We examine the 2-month data before MJO onset because the precursor

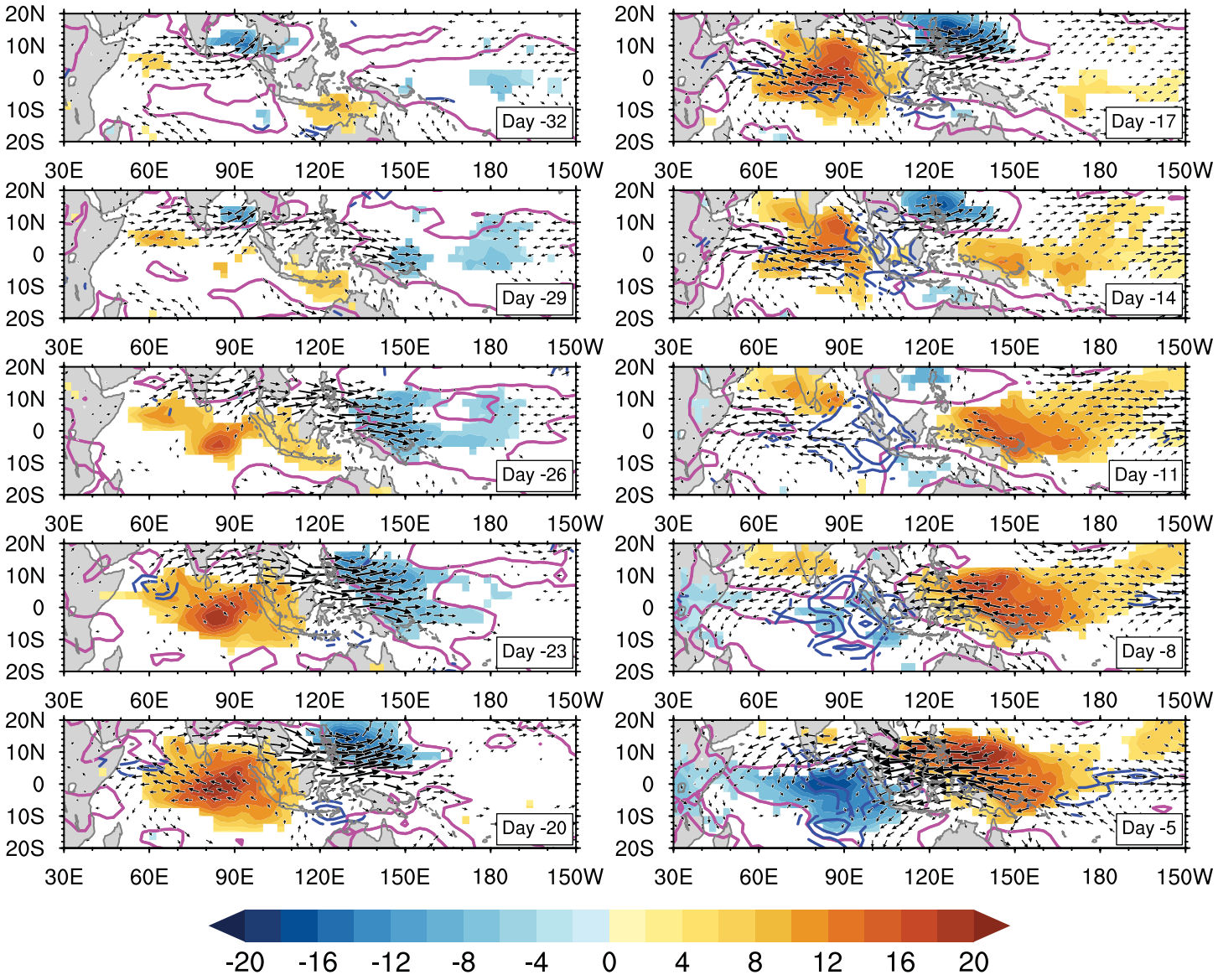

Fig. 3. Genesis processes of primary MJO in the WPISO cluster. Shown are the lagged composite of the 20–100-day filtered anomalies of OLR (shading; W m^{-2}), CWV (magenta contours; 0.05 g kg^{-1}), CWV tendency (blue contours; g kg^{-1} month^{-1}), and 850 hPa horizontal wind (vectors; m s^{-1}) from day −32 to day −5, with a time step of 3 days. For the CWV tendency, only positive anomalies are shown, with the contour interval of 0.3 g kg^{-1} month^{-1}. The shaded areas and vectors indicate significance passing the Student's *t* test at the 95% confidence level.

signals can be even observed, say the SD type, on day −60 (Fig. 1d). We also diagnosed the mean-state composites from −1 to 0 months, while the results were similar to those from −2 to 0 months (see Fig. ES7). The lag of 0 months denotes the month of MJO onset (covering day 0). Also, we composite the daily low-frequency (>100 days) anomalies before MJO onset, such as those from day −30 to day 5. Similar results are obtained for both methods.

For the WPISO cluster, there is a marked SST cooling over the tropical Pacific, with the maximum amplitude at the point of 0°, 140°W (Fig. 4a), which is reminiscent of the central Pacific (CP) type of La Niña events (Cai and Cowan 2009; Wei and Ren 2022). The negative SSTA is coupled with the zonally elongated easterly anomalies from the central to the western Pacific (Fig. 4e) and the reduced moist static energy (Fig. 4i) over the entire tropical Pacific. Since the trade wind strengthens during CP-type La Niña events, the occurrence frequency of the westward-propagating equatorial Rossby waves becomes more vigorous than the climatic average (Gonzalez and Jiang 2019), facilitating the WPISO-type MJO genesis. For the IOSC cluster, the composite background anomalies are generally small (Figs. 4b,f,j), although a

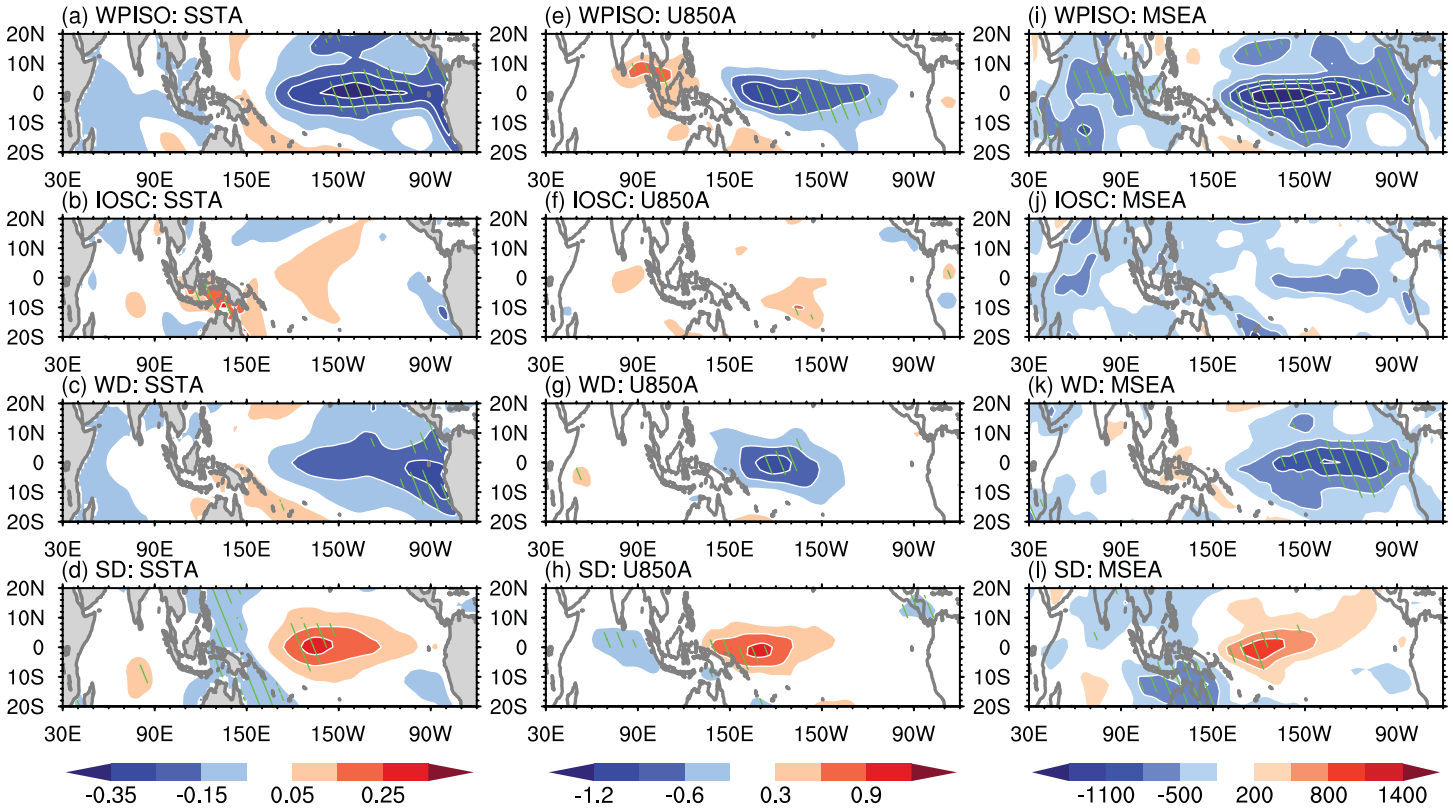

Fig. 4. Oceanic and atmospheric background states for diverse MJO genesis. Composite 3-month average anomalies (lags of –2 to 0 months) of the (a)–(d) sea surface temperature (SSTA; °C), (e)–(h) 850 hPa zonal wind (U850A; m s^{-1}), and (i)–(l) moist static energy (MSEA; J kg^{-1}) for the (a),(e),(i) WPISO-type; (b),(f),(j) IOSC-type; (c),(g),(k) WD-type; and (d),(h),(l) SD-type MJO genesis. The lag of 0 months denotes the month covering day 0, which indicates the date when the MJO convection reaches its peak over the IO. Significant anomalies passing the Student's *t* test at the 95% confidence level are hatched.

weak SST warming of about 0.1°C appears over the southern Maritime Continent. The weak dependence on the low-frequency background state suggests that the IOSC-type MJO genesis is probably less predictable.

The WD-type MJO genesis also corresponds to significant SST cooling in the tropical Pacific near the southern coast of the United States (Fig. 4c), similar to the eastern Pacific (EP) type of La Niña phenomenon. Unlike the WPISO cases, significant easterly wind anomaly is relatively confined to the date line region (Fig. 4g). In addition, the significant South Asian westerly wind anomaly associated with the WPISO (Fig. 3e) disappears in the case of the WD-type MJO genesis (Fig. 4g). All these features, for the comparison of the EP- and CP-type La Niña phenomena, are consistent with the findings of previous studies (Cai and Cowan 2009; Zhang et al. 2015; Wei and Ren 2022). The weakened intensity and reduced extent of wind anomalies give a plausible explanation for no strong WPISO in the EP-type La Niña phenomenon (Gonzalez and Jiang 2019). Moreover, the low moist static energy in the tropical Pacific Ocean (Fig. 4k) inhibits deep convection evolution, resulting in the weak dispersion of MJO genesis (Fig. 4c). In contrast, for the SD-type MJO genesis, the composite SSTA shows a CP-type El Niño phenomenon with SST warming peaking near the date line (Fig. 4d). Under this oceanic background state, the trade wind weakens (Fig. 4h) and the moist static energy increases (Fig. 4l), providing favorable conditions for the development of convection anomalies over the western Pacific. Thus, the strong dispersive MJO is preferable to occur before the MJO onset in the IO (Fig. 1d).

The above results suggest that climate models should be capable of simulating different ENSO flavors (Timmermann et al. 2018) well to characterize the diversity of MJO genesis. The successful simulation of the CP-type ENSO phenomena is particularly vital

for the occurrence of diverse MJO genesis in the IO. Moreover, the findings mentioned above show that diverse MJO genesis could be predicted by monitoring unique precursor signals under specific oceanic background states. The quasi-biennial oscillation (QBO) was recently found to have a large impact on the MJOs (Martin et al. 2021). Xiang et al. (2022) demonstrated that the slow-moving and stationary MJOs are prone to appear in easterly and westerly QBO phases, respectively. Here, we further found that easterly QBO also favors the SD-type MJO genesis, while in the other three types of MJO genesis, no obvious low-frequency background signals of the QBO were observed (Fig. ES8).

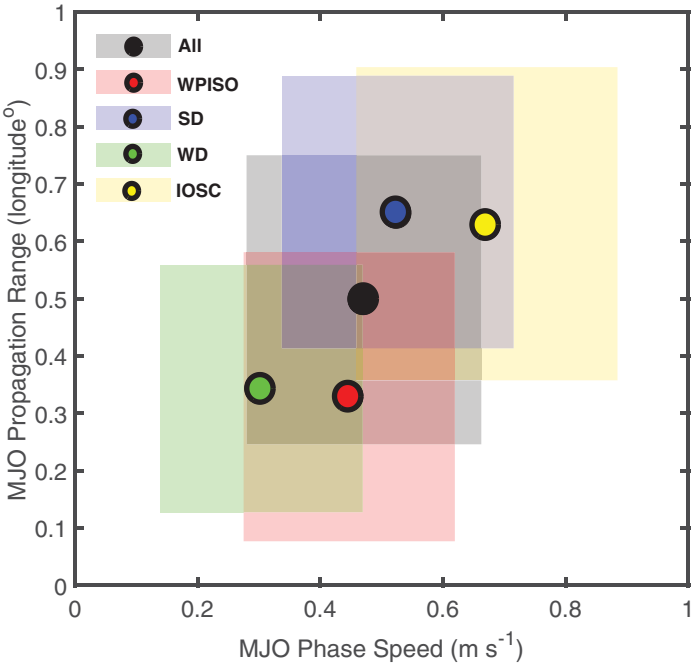

Fig. 5. Possible genesis–propagation link of MJO. Shown is the phase speed (m s^{-1}) vs zonal propagation range (longitude; °) of MJO events in the four MJO genesis types (red: WPISO; blue: SD; green: WD; yellow: IOSC) and also of all MJO cases (black). Appendix C details the methods to evaluate the phase speed and zonal range of any given MJO propagation in the latitude range of 15°S–15°N. The solid circles denote the sample mean, whose uncertainty range in one standard deviation is shaded in color.

Compared with Wang et al. (2019), we note that both the genesis and propagation types of MJO are influenced by the background SST anomalies. For example, the CP-type El Niño favors both fast MJO propagation and SD-type MJO genesis, and both the standing MJO and WPISO types have a CP La Niña–like background. A novel question is whether genesis and propagation are two independent features of the MJO or are linked? Here we consider attributing from two aspects of MJO propagation (see appendix C): phase speed (i.e., fast versus slow MJOs) and zonal propagation range (i.e., propagating versus standing MJOs). To facilitate comparison, the diagnosis of all MJOs is also included. The results suggest that the WPISO genesis type is likely followed by a standing MJO, while the IOSC type likely precedes a fast MJO with farther eastward propagation, as compared with all-case diagnosis (Fig. 5). For the other two types, a slow and standing MJO might follow the WD type, while a fast and propagating MJO is probably observed after the SD type. That the MJO is fast (slow) under a warm (cold) ENSO background was also reported in previous studies (e.g., Wei and Ren 2019; Lyu et al. 2021). These possible genesis–propagation links of MJO imply that different aspects of MJO might synergistically respond to the variations of low-frequency background states.

Prediction of diverse MJO genesis

Detecting possible windows of opportunity for skillful subseasonal prediction (especially on the time scale of 3–4 weeks) is a core task for implementing seamless forecasts (Hoskins 2013). In this study, we try to give a solution based on the classification of diverse MJO genesis in the IO. We select 10 subseasonal-to-seasonal prediction models (Vitart et al. 2017) that generate daily reforecasts data at a reforecast frequency of at least twice per month (Table ES1). To evaluate the predictions of MJO genesis, we calculate the RMM index of the reforecasts from each model. For simplicity, we directly show the multimodel mean skill of

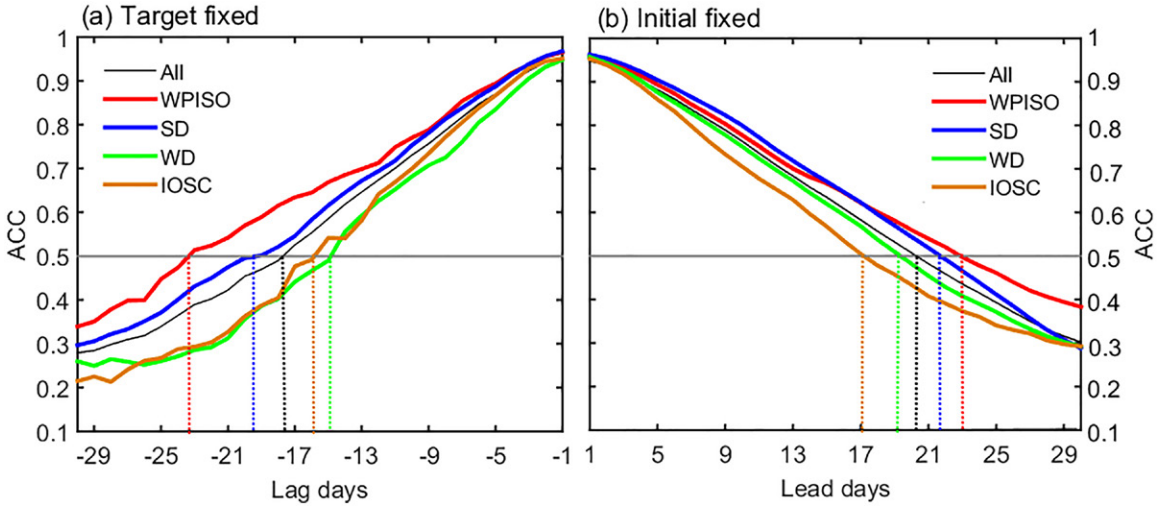

Fig. 6. Separable subseasonal prediction skills arising from MJO genesis diversity. (a) Anomaly correlation coefficient (ACC) as a function of lead day between observed and reforecasted RMM indices, with the target date fixed from days −5 to 5 of each MJO event for the WPISO (red)-, SD (blue)-, WD (green)-, and IOSC (brown)-type genesis. The black line presents the average results of all MJO cases, and the horizontal gray line highlights the ACC threshold of 0.5. (b) As in (a), but for the ACC with the initial date fixed from day −40 to −5.

the reforecasted RMM index, as shown in Fig. 6. The prediction skills of the individual models are in the supplemental material; see Fig. ES9.

First, we target the circulation and convection anomalies averaged from days −5 to 5 to investigate how predictable the eastward-propagating MJO onset is with different genesis types. The results suggest that the multimodel mean RMM skill of all MJO cases reaches 18 days, obtained when the anomaly correlation coefficient (ACC) drops below 0.5 (Fig. 6a). However, the prediction skills differ markedly for different types of MJO genesis. Specifically, the prediction skill for the WPISO type is the highest reaching about 24 days, which demonstrates that the primary MJO onset accompanied by a unique precursor signal of WPISO can be effectively predicted with fidelity even 3–4 weeks in advance. In the absence of this precursor signal, however, the prediction skill for the primary MJO onset is only about 16 days in terms of the IOSC type. For the successive MJO onset, the skill for the SD type is remarkably higher (~20 days) than that for the WD type (~15 days), suggesting a more predictable nature of the dispersive MJO. During the onset period of MJO deep convection, namely, days −5 to 5, the RMM values are a little different among the four clusters (Fig. 1), which may partially explain the differences in the prediction skill for the MJOs (Xiang et al. 2022). The noticeable easterly QBO phase in the SD cluster may also contribute to the higher skill for the SD type of successive MJO onset than the WD type (Martin et al. 2021).

Moreover, we specify the initial date to evaluate the reforecasted RMM index in the following 30 days. The initial date varies from days −40 to −5, namely, a period before the eastward-propagating MJO onset. In this scenario, the RMM prediction skill for all MJO cases becomes ~20 days (Fig. 6b). For the different types of MJO genesis, the prediction skills for the WPISO (~23 days) and SD (~22 days) types are increased by 2–3 days compared with the reference result of all MJO cases. In contrast, the skills for the WD and IOSC clusters decrease to approximately 19 and 17 days, respectively. Note that facilitated by westward-propagating precursor signals, the prediction skill for the primary WPISO-type MJOs increases by 6 days compared with that for the IOSC type. Moreover, the skill for the primary WPISO-type MJOs is higher than that for the successive SD-type MJOs as the forecast leading time lengthens, suggesting the particular significance of the WPISO signal for the MJO prediction at the leading time of 3–4 weeks. As shown in Fig. 1, the diversity of MJO genesis is also reflected in

different MJO intensity and propagation patterns, which may also affect the RMM skills of the individual MJO types.

Summary and discussions

Realistic simulation and accurate forecasts of the diversity of the MJOs are of great importance for the subseasonal-to-seasonal prediction of meteorological disasters (Wang et al. 2019; Xiang et al. 2022). Despite numerous studies on the diversity of MJO propagation, few have paid attention to the convective genesis before MJO onset. The systematic and quantitative analysis of the diversity of MJO genesis and their predictions will deepen our understanding of tropical dynamics and may help to detect a time window of opportunity for skillful prediction at the time scale of 3–4 weeks.

In this study, clustering analysis has been performed to classify the observed MJOs initiated from the IO into four types, namely, WPISO (20.4%), IOSC (15.4%), WD (25.9%), and SD (38.3%) types. The primary-type MJO genesis mostly occurred during the boreal summer, while the successive type preferred the boreal winter. The diverse MJO genesis was associated with different low-frequency oceanic and stratospheric background states. We detected a novel genesis-propagation link of MJO. For example, a standing MJO might follow the WPISO-type genesis, while a fast MJO was likely foreseen after the SD-type genesis. The findings could provide several guidelines for improving the simulation performance of models on the diversity of MJO genesis, thereby obtaining better subseasonal-to-seasonal predictions. The RMM prediction skills differed remarkably for the different types of MJO genesis. The most striking finding was that the newly detected WPISO precursor signals could improve the predictability (about 1 week) of the primary MJO onset. This result highlights the importance of capturing WPISO precursor signals in numerical weather and climate models for skillful subseasonal-to-seasonal prediction, particularly on the time scale of 3–4 weeks.

The primary MJO event investigated in Matthews (2008) was one that was preceded by local convection suppression over the IO, which is essentially the same as the IOSC-type MJO genesis investigated in this study. We further extended the work of Matthews (2008), i.e., we examined obvious WPISO precursor signals characterizing a portion of primary MJO events. The objective detection of the primary WPISO-type MJO onset is new and its scientific significance is twofold. First, it reveals a novel downstream initiation mechanism of primary MJO episodes, which is fundamentally different from previous studies that mostly emphasized the upstream effect and/or the extratropical forcing. The WPISO-type precursor signals can directly trigger the MJO deep convection through the merged moisture accumulation over the eastern IO. Additionally, the WPISO signals indirectly support the deep convection initiation through large-scale moisture advection processes. Second, the moist phase of the WPISO precursor might serve as a possible source of the suppressed convection over the IO and the western Pacific, which is robustly observed before primary MJO onset but its origin is previously unknown. Future work is necessary to quantify whether the westward-propagating wet signal could indeed trigger anomalous downward motions in the central-eastern IO using numerical sensitivity studies.

The major contrast between the two types of primary events is that the WPISO features MJO-scale moisture growth over both the western and eastern IO, while the IOSC type is triggered over the western IO. A further moisture budget analysis suggested that the western IO branch of convective initiation arises from the meridional moisture advection in both types (Fig. ES10). However, over the eastern IO, the moist convection of the WPISO type is triggered by the zonal moisture advection and also the wet phase of Rossby-wave-like disturbances.

The robust classification of successive MJO onset into WD and SD types is encouraging. Although the WD- and SD-type MJOs have similar triggering mechanisms, such as the circumnavigation of Kelvin waves, they prefer distinct background states and show noticeably

different predictability. For instance, the forecast leading time of the SD-type MJO onset is 4 days more than that of the WD type. The WD cluster can be treated as the canonical flavor of the MJOs since the new MJOs are successively generated over the IO with weak dispersion, which is also well simulated by most MJO theories (Zhang et al. 2020). The MJO is usually considered a nondispersive wave (Majda and Stechmann 2009; Wang et al. 2016). In this research, the objective extraction of the SD cluster without spatial filtering offers robust evidence to support the existence of westward energy dispersion in the observed MJO. The westward energy dispersion is a crucial feature predicted by the moisture-mode theory (Adames and Kim 2016). The results suggest that energy dispersion, as an essential characteristic of the MJOs that is previously less appreciated, deserves in-depth study in the future.

The background SST leading to the diversity of MJO genesis is similar to that causing the diversity of MJO propagation (Wang et al. 2019; Xiang et al. 2022). For example, the CP-type El Niño phenomenon favors both fast MJO propagation and SD-type MJO genesis, indicating that the MJO phase speed may depend on its energy dispersion. Also, the SD type is favored during the easterly QBO phase as a stratospheric background. These results implies that the multiple aspects of tropical convection (e.g., MJO) may synergistically respond to the change of climatic mean states. Moreover, how the MJO diversity in various aspects, such as propagation, dispersion, and genesis, will evolve under a warming climate is an open question and should be addressed through the joint efforts of our research community.

We believe that our findings presented in this study could serve as benchmarks for evaluating the modeling and prediction capabilities of contemporary weather and climate models. In the next step, it is necessary to assess the accuracy of the diverse MJO genesis simulated by the new generation of the Coupled Model Intercomparison Project, such as the CMIP6. Moreover, sensitivity experiments should be conducted for the simulations of numerical models to thoroughly evaluate the association of the diverse MJO genesis with the variations of low-frequency background states.

Acknowledgments. Thanks so much to the two anonymous reviewers that helped improve the paper. This work was jointly supported by the National Natural Science Foundation of China (Grants U2242206, 42288101, 41775066, 41905067, and 42175052) and the Basic Research and Operational Special Project of CAMS (Grant 2021Z007). We thank Dr. Bosong Zhang for his helpful comments and suggestions on improving the manuscript. We also acknowledge Dr. Shuo Zhao for helping download and pre-process the ERA5 data.

Data availability statement. Interpolated daily OLR data were obtained from the NOAA/OAR/ESRL PSD, Boulder, Colorado (https://psl.noaa.gov/thredds/catalog/Datasets/interp_OLR/catalog.html). NOAA_ERSST_V5 data were provided by the NOAA/OAR/ESRL PSL, Boulder, Colorado, from their website at https://psl.noaa.gov/data/gridded/data.noaa.ersst.v5.html. The ERA-Interim data were from https://climatedataguide.ucar.edu/climate-data/era-interim. The ERA5 data were available at https://cds.climate.copernicus.eu/#!/search?text=ERA5&type=dataset. OMI and RMM indices were from https://psl.noaa.gov/mjo/mjoindex/omi.1x.txt and http://www.bom.gov.au/climate/mjo/graphics/rmm.74toRealtime.txt, respectively. The subseasonal-to-seasonal reforecast data were achieved online (http://s2s.cma.cn).

Appendix A: Data introduction

The daily Advanced Very High-Resolution Radiometer (AVHRR) OLR data from the National Oceanic and Atmospheric Administration (NOAA; Liebmann and Smith 1996) are used to investigate the convective activities in the tropics. We use the ERA5 data from the European Centre for Medium-Range Weather Forecasts (Hersbach et al. 2020) to diagnose large-scale circulation. Previous studies have shown that the latest ERA5 data might produce

slightly stronger MJO than its predecessor, i.e., ERA-Interim (e.g., Bechtold et al. 2008; Ren et al. 2021). Both NOAA OLR and ERA5 data have a spatial resolution of 2.5° × 2.5° and a temporal coverage from 1979 to 2020. The global monthly SST is from the NOAA extended reconstructed SST version 5, with a horizontal resolution of 2° × 2° (Huang et al. 2017). Daily (monthly) anomalies are calculated by subtracting calendar daily (monthly) climatology. A 20–100-day bandpass Lanczos filter (Duchon 1979) with 201 weights is used to extract the intraseasonal signals from the daily anomalies. The observed OMI and RMM indexes are obtained online directly. Besides the observations, the reforecast data from 10 operational subseasonal-to-seasonal models (Vitart et al. 2017) are used to evaluate prediction skills for the MJO. The details are shown in Table ES1.

Appendix B: Classification of MJO genesis

Following the method introduced by Wei and Ren (2019) and Wei et al. (2022), we use the OMI1 to select possible MJO events originating from the IO. "Day 0" is identified when the standardized OMI1 (1980–2020) is larger than 1.0 and reaches a local maximum. An episode of MJO onset is further selected when the OMI amplitude is larger than 0.8 within 5 days after day 0. To exclude overlapping events, we set the time interval of the adjacent day 0 to exceed 25 days. The Hovmöller diagram of equatorially averaged (15°S–15°N), 20–100-day filtered OLR anomalies from days 0 to 40 is also examined for each event, to check whether an eastward-propagating MJO envelope (OLR anomaly < –10 W m^{-2}) indeed appears. In this way, we select a total of 201 MJO events in the IO during the past four decades. When the thresholds are slightly adjusted, e.g., the OMI amplitude > 0.9, the results of the study are stable, although the number of MJO events varies.

The genesis process and subsequent propagation of each MJO event can be tracked by using the Hovmöller diagrams of 20–100-day filtered OLR anomalies. We aim to identify the categories of genesis processes before the onset of MJO deep convection. Thus, a two-dimensional sample for each MJO event is obtained by using the meridionally average OLR (15°S–15°N) from days –30 to 0 with longitudes ranging from 45°E to 150°W. Nevertheless, a simple observation is difficult to classify the large ensemble unambiguously with more than 200 two-dimensional samples. Therefore, an unsupervised learning approach, the *k*-means clustering algorithm (Hartigan and Wong 1979), is adopted in the study to objectively classify the large ensemble into *k* representative clusters. In addition, the OLR anomalies are normalized along longitudes to make each sample comparable. Both positive and negative anomalies are input to the algorithm since both of them may affect the preconditioning stage of an MJO event. This input of the algorithm in this study is different from previous cases where only negative OLR anomalies were used to extract the diversity of MJO propagation (Wang et al. 2019). When *k* is greater than 4, a "new" cluster belonging to the successive type of MJO initiation is always obtained, while it is an "old" cluster that has been already isolated at $k = 4$. To facilitate the readers, the clustering results of $k = 3$, 5, and 6 are also shown in the online supplemental file (i.e., Figs. ES11–ES13). One can see that no new cluster in terms of the MJO initiation manner can be obtained when *k* is increased, although the details in the composite MJO propagation pattern may differ slightly due to the change in the number of MJO events. Therefore, $k = 4$ is chosen as the optimal cluster number in this study.

Appendix C: Evaluating phase speed and zonal propagation range of MJO

For each MJO event initiated on day 0, we consider the time–longitude section of 60°E–120°W, days –10 to 40. The enhanced convective regions are defined as 20–100-day filtered OLR anomalies less than –10 W m^{-2}, which approaches the globally averaged standard deviation of filtered OLR anomalies in 15°S–15°N. For example, for the MJO episode

initiated on 14 January 1993, three convective regions have been identified (labeled as A, B, and C in Fig. C1). A belongs to this MJO since continuously eastward-propagating convection is observed. B or C, which disconnects with A, can be treated as the same MJO only if (i) the zonal distance between its center and the rightmost edge of A is less than 25° and also (ii) the time interval between its center and the uppermost edge of A is less than 10 days. The slight changes in these two parameters do not change the results of this study. Accordingly, one can easily identify A as the main body of this MJO, while B and C are not. Besides, the rightmost position (in longitude) of the eastward propagation for this MJO is also obtained (see the red solid line in Fig. C1). Next, we divide the space ranging from 60°E to the MJO rightmost position into 10° segments with 10° overlap. The 20–100-day filtered OLR anomalies are averaged in each segment, and we then identify the minimum in the time series from days −5 to 30. These local minima are marked in Fig. C1. The phase speed is evaluated as the linear square fit of these white circles. The zonal propagation range is the distance from the day 0 longitude to the rightmost position.

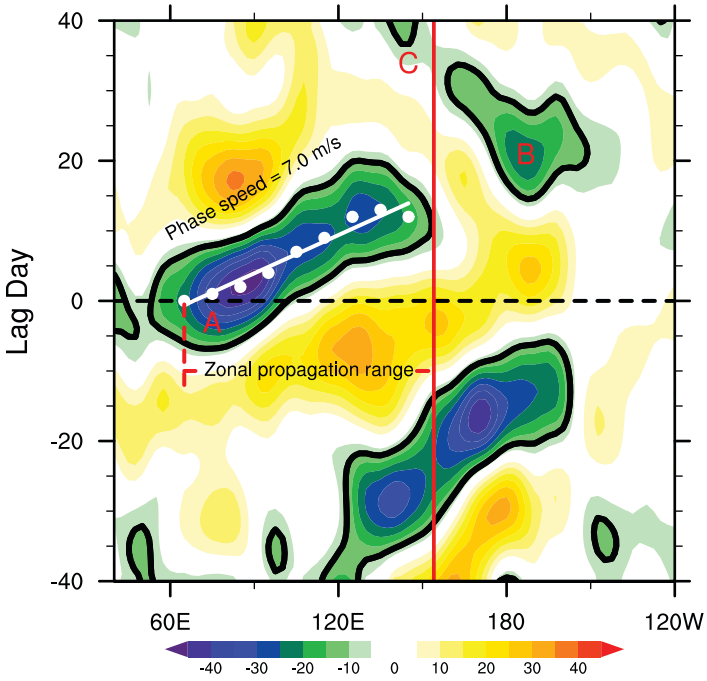

Fig. C1. Schematic diagram illustrating the methods to evaluate MJO phase speed and zonal propagation range. Lead–lag evolution of 20–100-day filtered OLR anomalies (15°S–15°N average) with day 0 denoting 14 January 1993. The solid red line denotes the rightmost position (in longitude) of MJO eastward propagation, which is identified when the threshold value of −10 W m^{-2} (black contours) is met. The white circles show the local minima during days −5 to 30 and from 60°E to the rightmost position (~154°E). The longitude range (60°–154°E) is segmented into intervals of 10 longitudes with an overlap of 10 longitudes. The white line denotes the linear least squares fit of the white circles. Letters A, B, and C mark the enhanced convective regions (i.e., <−10 W m^{-2}).

References

Adames, Á. F., and D. Kim, 2016: The MJO as a dispersive, convectively coupled moisture wave: Theory and observations. *J. Atmos. Sci.*, **73**, 913–941, https://doi.org/10.1175/JAS-D-15-0170.1.

Bechtold, P., M. Köhler, T. Jung, F. Doblas-Reyes, M. Leutbecher, M. J. Rodwell, F. Vitart, and G. Balsamo, 2008: Advances in simulating atmospheric variability with the ECMWF model: From synoptic to decadal time-scales. *Quart. J. Roy. Meteor. Soc.*, **134**, 1337–1351, https://doi.org/10.1002/qj.289.

Bellenger, H., and J. P. Duvel, 2012: The event-to-event variability of the boreal winter MJO. *Geophys. Res. Lett.*, **39**, L08701, https://doi.org/10.1029/2012GL051294.

Cai, W., and T. Cowan, 2009: La Niña Modoki impacts Australia autumn rainfall variability. *Geophys. Res. Lett.*, **36**, L12805, https://doi.org/10.1029/2009GL037885.

Cassou, C., 2008: Intraseasonal interaction between the Madden–Julian oscillation and the North Atlantic Oscillation. *Nature*, **455**, 523–527, https://doi.org/10.1038/nature07286.

Duchon, C. E., 1979: Lanczos filtering in one and two dimensions. *J. Appl. Meteor.*, **18**, 1016–1022, https://doi.org/10.1175/1520-0450(1979)018<1016:LFIOAT>2.0.CO;2.

Feng, J., and T. Li, 2016: Initiation mechanisms for a successive MJO event and a primary MJO event during boreal winter of 2000–2001. *J. Trop. Meteor.*, **22**, 479–496, https://doi.org/10.16555/j.1006-8775.2016.04.004.

Garfinkel, C. I., S. B. Feldstein, D. W. Waugh, C. Yoo, and S. Lee, 2012: Observed connection between stratospheric sudden warmings and the Madden–Julian oscillation. *Geophys. Res. Lett.*, **39**, L18807, https://doi.org/10.1029/2012GL053144.

Gonzalez, A. O., and X. Jiang, 2019: Distinct propagation characteristics of intraseasonal variability over the tropical west Pacific. *J. Geophys. Res. Atmos.*, **124**, 5332–5351, https://doi.org/10.1029/2018JD029884.

Hartigan, J. A., and M. A. Wong, 1979: Algorithm AS 136: A *K*-means clustering algorithm. *Appl. Stat.*, **28**, 100–108, https://doi.org/10.2307/2346830.

Hendon, H. H., and B. Liebmann, 1990: The intraseasonal (30–50 day) oscillation of the Australian summer monsoon. *J. Atmos. Sci.*, **47**, 2909–2924, https://doi.org/10.1175/1520-0469(1990)047<2909:TIDOOT>2.0.CO;2.

Hersbach, H., and Coauthors, 2020: The ERA5 global reanalysis. *Quart. J. Roy. Meteor. Soc.*, **146**, 1999–2049, https://doi.org/10.1002/qj.3803.

Hoskins, B., 2013: The potential for skill across the range of the seamless weather-climate prediction problem: A stimulus for our science. *Quart. J. Roy. Meteor. Soc.*, **139**, 573–584, https://doi.org/10.1002/qj.1991.

Hsu, P.-C., Z. Fu, H. Murakami, J.-Y. Lee, C. Yoo, N. C. Johnson, C.-H. Chang, and Y. Liu, 2021: East Antarctic cooling induced by decadal changes in Madden–Julian oscillation during austral summer. *Sci. Adv.*, **7**, eabf9903, https://doi.org/10.1126/sciadv.abf9903.

Huang, B., and Coauthors, 2017: Extended Reconstructed Sea Surface Temperature, Version 5 (ERSSTv5): Upgrades, Validations, and Intercomparisons. *J. Climate*, **30**, 8179–8205, https://doi.org/10.1175/JCLI-D-16-0836.1.

Jiang, X., and Coauthors, 2020: Fifty years of research on the Madden–Julian oscillation: Recent progress, challenges, and perspectives. *J. Geophys. Res. Atmos.*, **125**, e2019JD030911, https://doi.org/10.1029/2019JD030911.

Kemball-Cook, S., and B. Weare, 2001: The onset of convection in the Madden–Julian oscillation. *J. Climate*, **14**, 780–793, https://doi.org/10.1175/1520-0442(2001)014<0780:TOOCIT>2.0.CO;2.

Kiladis, G., J. D., K. H. Straub, M. C. Wheeler, S. N. Tulich, K. Kikuchi, K. M. Weickmann, and M. J. Ventrice, 2014: A comparison of OLR and circulation-based indices for tracking the MJO. *Mon. Wea. Rev.*, **142**, 1697–1715, https://doi.org/10.1175/MWR-D-13-00301.1.

Kim, D., J.-S. Kug, and A. H. Sobel, 2014: Propagating versus nonpropagating Madden–Julian oscillation events. *J. Climate*, **27**, 111–125, https://doi.org/10.1175/JCLI-D-13-00084.1.

Lau, K. M., and P. H. Chan, 1986: Aspects of the 40–50 day oscillation during the northern summer as inferred from outgoing longwave radiation. *Mon. Wea. Rev.*, **114**, 1354–1367, https://doi.org/10.1175/1520-0493(1986)114<1354:AOTDOD>2.0.CO;2.

Li, T., F. Tam, X. Fu, Z. T.-J. Zhou, and W.-J. Zhu, 2008: Causes of the intraseasonal SST variability in the tropical Indian Ocean. *Atmos. Ocean Sci. Lett.*, **1**, 18–23, https://doi.org/10.1080/16742834.2008.11446758.

Liebmann, B., and C. A. Smith, 1996: Description of a complete (interpolated) outgoing longwave radiation dataset. *Bull. Amer. Meteor. Soc.*, **77**, 1275–1277, https://doi.org/10.1175/1520-0477-77.6.1274.

——, H. H. Hendon, and J. D. Glick, 1994: The relationship between tropical cyclones of the western Pacific and Indian Oceans and the Madden–Julian oscillation. *J. Meteor. Soc. Japan*, **72**, 401–412, https://doi.org/10.2151/jmsj1965.72.3_401.

Lyu, M., X. Jiang, Z. Wu, D. Kim, and Á. F. Adames, 2021: Zonal-scale of the Madden–Julian oscillation and its propagation speed on the interannual time-scale. *Geophys. Res. Lett.*, **48**, e2020GL091239, https://doi.org/10.1029/2020GL091239.

Madden, R. A., and P. R. Julian, 1971: Detection of a 40–50 day oscillation in the zonal wind in the tropical Pacific. *J. Atmos. Sci.*, **28**, 702–708, https://doi.org/10.1175/1520-0469(1971)028<0702:DOADOI>2.0.CO;2.

——, and ——, 1972: Description of global-scale circulation cells in the tropics with a 40–50 day period. *J. Atmos. Sci.*, **29**, 1109–1123, https://doi.org/10.1175/1520-0469(1972)029<1109:DOGSCC>2.0.CO;2.

Majda, A. J., and S. N. Stechmann, 2009: The skeleton of tropical intraseasonal oscillations. *Proc. Natl. Acad. Sci. USA*, **106**, 8417–8422, https://doi.org/10.1073/pnas.0903367106.

Maloney, E. D., and D. L. Hartmann, 2000: Modulation of hurricane activity in the Gulf of Mexico by the Madden–Julian oscillation. *Science*, **287**, 2002–2004, https://doi.org/10.1126/science.287.5460.2002.

Mariotti, A., and Coauthors, 2020: Windows of opportunity for skillful forecasts subseasonal to seasonal and beyond. *Bull. Amer. Meteor. Soc.*, **101**, E608–E625, https://doi.org/10.1175/BAMS-D-18-0326.1.

Martin, Z., and Coauthors, 2021: The influence of the quasi-biennial oscillation on the Madden–Julian oscillation. *Nat. Rev. Earth Environ.*, **2**, 477–489, https://doi.org/10.1038/s43017-021-00173-9.

Matsueda, S., and Y. Takaya, 2015: The global influence of the Madden–Julian oscillation on extreme temperature events. *J. Climate*, **28**, 4141–4151, https://doi.org/10.1175/JCLI-D-14-00625.1.

Matthews, A. J., 2000: Propagation mechanisms for the Madden–Julian Oscillation. *Quart. J. Roy. Meteor. Soc.*, **126**, 2637–2651, https://doi.org/10.1002/qj.49712656902.

——, 2008: Primary and successive events in the Madden–Julian oscillation. *Quart. J. Roy. Meteor. Soc.*, **134**, 439–453, https://doi.org/10.1002/qj.224.

——, and G. N. Kiladis, 1999: The tropical–extratropical interaction between high-frequency transients and the Madden–Julian oscillation. *Mon. Wea. Rev.*, **127**, 661–677, https://doi.org/10.1175/1520-0493(1999)127<0661:TTEIBH>2.0.CO;2.

McPhaden, M. J., 1999: Genesis and evolution of the 1997–98 El Niño. *Science*, **283**, 950–954, https://doi.org/10.1126/science.283.5404.950.

Moum, J. N., K. Pujiana, R.-C. Lien, and W. D. Smyth, 2016: Ocean feedback to pulses of the Madden–Julian oscillation in the equatorial Indian Ocean. *Nat. Commun.*, **7**, 13203, https://doi.org/10.1038/ncomms13203.

Mundhenk, B. D., E. A. Barnes, E. D. Maloney, and C. F. Baggett, 2018: Skillful empirical subseasonal prediction of landfalling atmospheric river activity using the Madden–Julian oscillation and quasi-biennial oscillation. npj Climate *Atmos. Sci.*, **1**, 20177, https://doi.org/10.1038/s41612-017-0008-2.

Nakazawa, T., 1988: Tropical super clusters within intraseasonal variations over the western Pacific. *J. Meteor. Soc. Japan*, **66**, 823–839, https://doi.org/10.2151/jmsj1965.66.6_823.

Pohl, B., and P. Camberlin, 2014: A typology for intraseasonal oscillations. *Int. J. Climatol.*, **34**, 430–445, https://doi.org/10.1002/joc.3696.

Rao, S. A., and T. Yamagata, 2004: Abrupt termination of Indian Ocean dipole events in response to intraseasonal disturbances. *Geophys. Res. Lett.*, **31**, L19306, https://doi.org/10.1029/2004GL020842.

Ren, H.-L., and P. Ren, 2017: Impact of Madden–Julian Oscillation upon winter extreme rainfall in Southern China: Observations and predictability in CFSv2. *Atmosphere*, **8**, 192, https://doi.org/10.3390/atmos8100192.

Ren, P., D. Kim, M. Ahn, D. Kang, and H.-L. Ren, 2021: Intercomparison of MJO column moist static energy and water vapor budget among six modern reanalysis products. *J. Climate*, **34**, 2977–3001, https://doi.org/10.1175/JCLI-D-20-0653.1.

Snide, C. E., Á. F. Adames, S. W. Powell, and V. C. Mayta, 2021: The role of large-scale moistening by adiabatic lifting in the Madden–Julian oscillation convective onset. *J. Climate*, **35**, 269–284, https://doi.org/10.1175/JCLI-D-21-0322.1.

Sobel, A. H., and E. Maloney, 2013: Moisture modes and the eastward propagation of the MJO. *J. Atmos. Sci.*, **70**, 187–192, https://doi.org/10.1175/JAS-D-12-0189.1.

Stachnik, J. P., and B. Chrisler, 2020: An index intercomparison for MJO events and termination. *J. Geophys. Res. Atmos.*, **125**, e2020JD032507, https://doi.org/10.1029/2020JD032507.

Straub, K. H., 2013: MJO initiation in the real-time multivariate MJO index. *J. Climate*, **26**, 1130–1151, https://doi.org/10.1175/JCLI-D-12-00074.1.

——, G. N. Kiladis, and P. E. Ciesielski, 2006: The role of equatorial waves in the onset of the South China Sea summer monsoon and the demise of El Niño during 1998. *Dyn. Atmos. Oceans*, **42**, 216–238, https://doi.org/10.1016/j.dynatmoce.2006.02.005.

Takasuka, D., and M. Satoh, 2021: Diversity of the Madden–Julian oscillation: Initiation region modulated by the interaction between the intraseasonal and interannual variabilities. *J. Climate*, **34**, 2297–2318, https://doi.org/10.1175/JCLI-D-20-0688.1.

——, ——, T. Miyakawa, and H. Miura, 2018: Initiation processes of the tropical intraseasonal variability simulated in an aqua-planet experiment: What is the intrinsic mechanism for MJO onset? *J. Adv. Model. Earth Syst.*, **10**, 1047–1073, https://doi.org/10.1002/2017MS001243.

——, ——, and S. Yokoi, 2019: Observational evidence of mixed Rossby-gravity waves as a driving force for the MJO convective initiation and propagation. *Geophys. Res. Lett.*, **46**, 5546–5555, https://doi.org/10.1029/2019GL083108.

——, T. Kohyama, H. Miura, and T. Suematsu, 2021: MJO initiation triggered by amplification of upper-tropospheric dry mixed Rossby-gravity waves. *Geophys. Res. Lett.*, **48**, e2021GL094239, https://doi.org/10.1029/2021GL094239.

Takayabu, Y., T. Iguchi, M. Kachi, A. Shibata, and H. Kanzawa, 1999: Abrupt termination of the 1997–98 El Niño in response to a Madden–Julian oscillation. *Nature*, **402**, 279–282, https://doi.org/10.1038/46254.

Timmermann, A., and Coauthors, 2018: El Niño–Southern Oscillation complexity. *Nature*, **559**, 535–545, https://doi.org/10.1038/s41586-018-0252-6.

Vitart, F., and Coauthors, 2017: The Subseasonal to Seasonal (S2S) Prediction Project Database. *Bull. Amer. Meteor. Soc.*, **98**, 163–173, https://doi.org/10.1175/BAMS-D-16-0017.1.

Waliser, D. E., K. M. Lau, W. Stern, and C. Jones, 2003: Potential predictability of the Madden–Julian oscillation. *Bull. Amer. Meteor. Soc.*, **84**, 33–50, https://doi.org/10.1175/BAMS-84-1-33.

——, and Coauthors, 2012: The "year" of tropical convection (May 2008–April 2010): Climate variability and weather highlights. *Bull. Amer. Meteor. Soc.*, **93**, 1189–1218, https://doi.org/10.1175/2011BAMS3095.1.

Wang, B., F. Liu, and G. Chen, 2016: A trio-interaction theory for Madden–Julian oscillation. *Geosci. Lett.*, **3**, 34, https://doi.org/10.1186/s40562-016-0066-z.

——, G. Chen, and F. Liu, 2019: Diversity of the Madden–Julian oscillation. *Sci. Adv.*, **5**, eaax0220, https://doi.org/10.1126/sciadv.aax0220.

Wang, Y., H.-L. Ren, Y. Wei, F.-F. Jin, P. Ren, L. Gao, and J. Wu, 2022: MJO phase swings modulate the recurring latitudinal shifts of the 2020 extreme summer-monsoon rainfall around Yangtse. *J. Geophys. Res. Atmos.*, **127**, e2021JD036011, https://doi.org/10.1029/2021JD036011.

Webber, B. G., A. J. Matthews, and K. J. Heywood, 2010: A dynamical ocean feedback mechanism for the Madden–Julian oscillation. *Quart. J. Roy. Meteor. Soc.*, **136**, 740–754, https://doi.org/10.1002/qj.604.

Wei, Y., and H.-L. Ren, 2019: Modulation of ENSO on fast and slow MJO modes during boreal winter. *J. Climate*, **32**, 7483–7506, https://doi.org/10.1175/JCLI-D-19-0013.1.

——, and Z. Pu, 2021: Diurnal cycle of precipitation and near-surface atmospheric conditions over the maritime continent: Land–sea contrast and impacts of ambient winds in cloud-permitting simulations. *Climate Dyn.*, **58**, 2421–2449, https://doi.org/10.1007/s00382-021-06012-3.

——, and H.-L. Ren, 2022: Distinct MJOs under the two types of La Niña. *J. Geophys. Res. Atmos.*, **127**, e2022JD037646, https://doi.org/10.1029/2022JD037646.

——, M. Mu, H.-L. Ren, and J.-X. Fu, 2019: Conditional nonlinear optimal perturbations of moisture triggering primary MJO initiation. *Geophys. Res. Lett.*, **46**, 3492–3501, https://doi.org/10.1029/2018GL081755.

——, H.-L. Ren, M. Mu, and J.-X. Fu, 2020: Nonlinear optimal moisture perturbations as excitation of primary MJO events in a hybrid coupled climate model. *Climate Dyn.*, **54**, 675–699, https://doi.org/10.1007/s00382-019-05021-7.

——, F. Liu, H.-L. Ren, G. Chen, C. Feng, and B. Chen, 2022: Western Pacific premoistening for eastward-propagating BSISO and its ENSO modulation. *J. Climate*, **35**, 4979–4996, https://doi.org/10.1175/JCLI-D-21-0923.1.

Wheeler, M., and G. N. Kiladis, 1999: Convectively coupled equatorial waves: Analysis of clouds and temperature in the wavenumber–frequency domain. *J. Atmos. Sci.*, **56**, 374–399, https://doi.org/10.1175/1520-0469(1999)056<0374:CCEWAO>2.0.CO;2.

——, and H. Hendon, 2004: An all-season real-time multivariate MJO index: Development of an index for monitoring and prediction. *Mon. Wea. Rev.*, **132**, 1917–1932, https://doi.org/10.1175/1520-0493(2004)132<1917:AARMMI>2.0.CO;2.

Xiang, B., and Coauthors, 2022: S2S prediction in GFDL SPEAR: MJO diversity and teleconnections. *Bull. Amer. Meteor. Soc.*, **103**, E463–E484, https://doi.org/10.1175/BAMS-D-21-0124.1.

Xie, Y.-B., S.-J. Chen, I.-L. Zhang, and Y.-L. Hung, 1963: A preliminarily statistic and synoptic study about the basic currents over southeastern Asia and the initiation of typhoon. *Acta Meteor. Sin.*, **33**, 206–217, https://doi.org/10.1007/s13351-018-8888-6.

Yang, D., and A. P. Ingersoll, 2013: Triggered convection, gravity waves, and the MJO: A shallow-water model. *J. Atmos. Sci.*, **70**, 2476–2486, https://doi.org/10.1175/JAS-D-12-0255.1.

Yang, G. Y., and J. Slingo, 2001: The diurnal cycle in the tropics. *Mon. Wea. Rev.*, **129**, 784–801, https://doi.org/10.1175/1520-0493(2001)129<0784:TDCITT>2.0.CO;2.

Yasunari, T., 1980: A quasi-stationary appearance of 30 to 40 day period in the cloudiness fluctuations during the summer monsoon over India. *J. Meteor. Soc. Japan*, **58**, 225–229, https://doi.org/10.2151/jmsj1965.58.3_225.

Yoneyama, K., C. Zhang, and C. Long, 2013: Tracking pulses of the Madden–Julian oscillation. *Bull. Amer. Meteor. Soc.*, **94**, 1871–1891, https://doi.org/10.1175/BAMS-D-12-00157.1.

Yong, Y., and J. Mao, 2016: Mechanistic analysis of the suppressed convective anomaly precursor associated with the initiation of primary MJO events over the tropical Indian Ocean. *Climate Dyn.*, **46**, 779–795, https://doi.org/10.1007/s00382-015-2612-3.

Zhang, C., 2005: Madden–Julian oscillation. *Rev. Geophys.*, **43**, RG2003, https://doi.org/10.1029/2004RG000158.

——, 2013: Madden–Julian oscillation: Bridging weather and climate. *Bull. Amer. Meteor. Soc.*, **94**, 1849–1870, https://doi.org/10.1175/BAMS-D-12-00026.1.

——, and J. Ling, 2017: Barrier effect of the Indo-Pacific Maritime Continent on the MJO: Perspectives from tracking MJO precipitation. *J. Climate*, **30**, 3439–3459, https://doi.org/10.1175/JCLI-D-16-0614.1.

——, and K. Yoneyama, 2017: CINDY/DYNAMO field campaign: Advancing our understanding of MJO initiation. *The Global Monsoon System: Research and Forecast*, 3rd ed. C.-P. Chang et al., Eds., World Scientific, 339–348, https://doi.org/10.1142/9789813200913_0027.

——, Á. F. Adames, B. Khouider, B. Wang, and D. Yang, 2020: Four theories of the Madden–Julian oscillation. *Rev. Geophys.*, **58**, e2019RG000685, https://doi.org/10.1029/2019RG000685.

Zhang, W., L. Wang, B. Xiang, L. Qi, and J. He, 2015: Impacts of two types of La Niña on the NAO during boreal winter. *Climate Dyn.*, **44**, 1351–1366, https://doi.org/10.1007/s00382-014-2155-z.

Zhao, C., T. Li, and T. Zhou, 2013: Precursor signals and processes associated with MJO initiation over the tropical Indian Ocean. *J. Climate*, **26**, 291–307, https://doi.org/10.1175/JCLI-D-12-00113.1.

Zhou, W., D. Yang, S.-P. Xie, and J. Ma, 2020: Amplified Madden–Julian oscillation impacts in the Pacific–North America region. *Nat. Climate Change*, **10**, 654–660, https://doi.org/10.1038/s41558-020-0814-0.